BAYESIAN CONSIDERATION OF THE TOMOGRAPHY PROBLEM

W. von der Linden, K. Ertl, and V. Dose
Max-Planck-Institut für Plasmaphysik, EURATOM Association
D-85740 Garching b. München, Germany
e-mail: wvl@ibmop5.ipp-garching.mpg.de

ABSTRACT. Soft X-ray tomography has become a standard diagnostic equipment to investigate plasma profiles. Due to limitations in viewing-access and detector numbers the reconstruction of the two-dimensional emissivity profile constitutes a highly underdetermined inversion problem. We discuss the principle features of the tomography problem from the Bayesian point of view in various stages of sophistication. The approach is applied to real-world data obtained from the Wendelstein 7AS stellerator.

1. Introduction

Soft X-ray emission tomography is used to analyze the formation and time-evolution of the poloidal plasma cross-section on tokamaks and stellerators. It depends on various plasma parameters, like temperature, density and effective atomic number. The knowledge of the emissivity profile allows to infer to some extent internal properties of the plasma, like position, shape, impurity distribution, and magneto-hydrodynamic (MHD) modes. Typically, a set of detectors is used as depicted in fig.1 to record X-rays emitted by the plasma. A

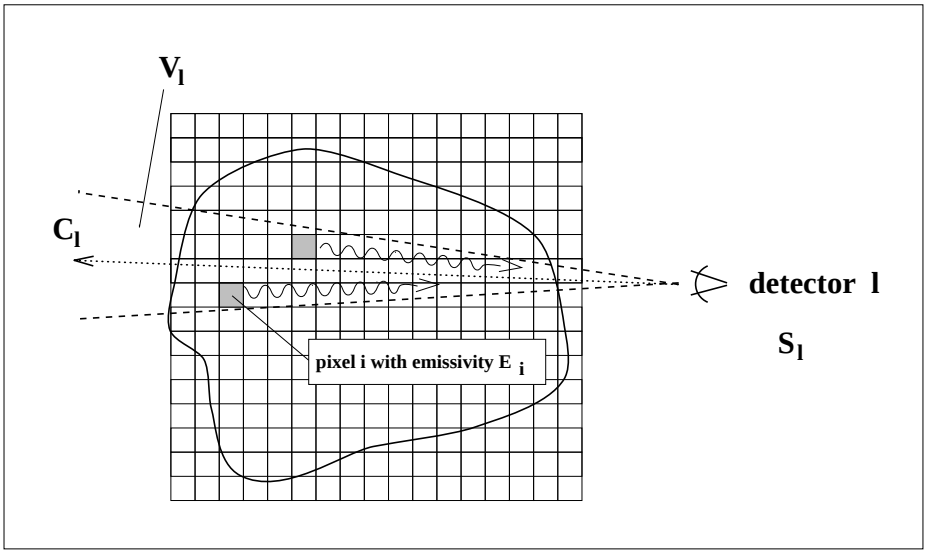

Figure 1: *X-ray tomography*

plasma in the temperature and density range of interest is optically thin for X-rays, so

radiation from internal points of the plasma, say pixel i, reaches the detectors without absorption. Hence, the signal S_l, recorded by detector l, is the integrated emissivity of all pixels lying in viewing cone V_l, formed by the detector and the collimator aperture

$$S_l(E) = \sum_{i \epsilon V_l} g_{li} E_i \qquad . \tag{1}$$

In addition, the signal is deteriorated by experimental errors σ_l. The matrix g_{li} contains: a) the physics of X-rays such as the $1/r^2$ intensity-fall off. b) the geometry of the detector arrangement. In particular the r^2 increase in volume, which cancels the aforementioned $1/r^2$-decrease. c) characteristics of detector l such as sensitivity etc.. A thorough determination of g_{li} is an essential part of the tomography problem. An incompatible g, used to invert Eq.1, would lead to significant artifacts in the emissivity profile. Such problems are absent when using artificial test data, which limits the value of simulations with synthetic data.

2. Qualitative discussion

In order to analyze the experimental data we employed the most accurate values for g_{li} we could get. For a qualitative discussion, however, it is expedient to use a widespread approximation

$$S_l(E) = g \int_{C_l} E(\vec{x}) ds \qquad , \tag{2}$$

which is justified if the solid angle of the viewing-cones is very narrow, the spatial extent of the detector slit is much smaller than the plasma diameter, and if all detectors have identical sensitivities. In this case, signal S_l is proportional to the line-integrated emissivity along the view-chord C_l. For the qualitative discussion we assume pixels on a square-lattice, as depicted in fig.1. Furthermore, we take the liberty to install detectors viewing parallel to the x- and y-axis, respectively, such that the mid-point of each pixel is intersected by 2 orthogonal viewing-chords. Put differently, the viewing-chords constitute a square-lattice which is shifted relative to the pixel-mesh by half a unit-cell diagonal. In this case, Eq.2 simplifies to

$$S_i^x = \tilde{g} \sum_j E_{ij} \qquad ; \qquad S_j^y = \tilde{g} \sum_i E_{ij} \qquad . \tag{3}$$

$S_i^{(x/y)}$ stands for the signal recorded by detector i along the (x/y)-axis and E_{ij} represents the emissivity of the pixel at position (i,j) on the square-lattice. The inversion of Eq.3 is ill-posed, which is most easily seen in the case of 2x2 pixels and 2+2 detectors. In this case the linear problem can be written as

$$\vec{S} = \tilde{g} \begin{pmatrix} 1 & 1 & 0 & 0 \\ 0 & 0 & 1 & 1 \\ 1 & 0 & 1 & 0 \\ 0 & 1 & 0 & 1 \end{pmatrix} \vec{E} \; = \; G\vec{E} \qquad . \tag{4}$$

Obviously, Eq.4 has no unique solution since $\det(G) = 0$. The reason is that viewing-chords are provided for only two angles. It is of no use to install an infinite number of detectors along the two axes; the inversion would remain underdetermined. For a unique

solution a complete coverage of all angles is required. This point becomes apparent when employing the Fourier transform in polar coordinates [1, 2, 3, 4]. A first insight into the tomography problem can be obtained by ignoring experimental errors and assuming that the total emissivity is known $E_0 = \sum_{ij} E_{ij}$. It is advantageous to express the emissivity in terms of a probability distribution $p_{ij} = E_{ij}/E_0$ which we determine in the frame of Jaynes' MaxEnt[5]. The data-constraints are simply

$$s_i^x = \sum_j p_{ij} \quad ; \quad s_j^y = \sum_i p_{ij} \quad ; \quad 1 = \sum_{ij} p_{ij} \quad , \tag{5}$$

with $s_i^{(x/y)} = S_i^{(x/y)}/(E_0\tilde{g})$. The entropy $\mathcal{S} = -\sum_{ij} p_{ij} \ln p_{ij}$ is maximized subject to the data-constraints which amounts to maximizing the Lagrangian

$$\mathcal{L} = -\sum_{ij} p_{ij} \ln p_{ij} - \sum_i \lambda_i^x (\sum_j p_{ij} - s_i^x) - \sum_j \lambda_j^y (\sum_i p_{ij} - s_j^y) - \lambda_0 (\sum_{ij} p_{ij} - 1) \tag{6}$$

with respect to p_{ij} and the Lagrange parameters λ. The MaxEnt result reads

$$E_{ij} \propto s_i^x * s_j^y \quad , \tag{7}$$

Since the "experimental" geometry provides no correlation between x- and y-detector signals and due to MaxEnt's maxim of being unbiased, the x- and y-components of the resulting emissivity are uncorrelated. This will be different in the real world experiment which introduces correlation as we will see below. The orthogonal viewing-geometry leads to a significant restriction in angular resolution. This point is elucidated in table 1, where a few examples for a 3x3 pixel-field with 3+3 detectors are provided. The left panel depicts possible solutions of the ambiguous inversion problem, while the right panel shows the unique MaxEnt solution. Obviously, MaxEnt yields the most symmetric solution, as far as point transformations and translations are concerned. To increase the angular resolution a set of rotated reference-frames is required. This has been achieved, despite of the rather limited viewing-access, in the Wendelstein stellerator W7AS as follows. In order to image the poloidal emissivity profile two sets of detector-arrays are used. Each array consists of 36 detectors. The radiation is collimated in both detector-arrays by rectangular slits which produce a fan-like view-configuration as depicted in fig2. This geometry is probably the most useful for wide-angle viewing in situations with restricted access. As the next step towards the solution of the realistic tomography problem, we use the fan-like geometry. Still ignoring experimental errors and employing the line-integral approximation Eq.2 we obtain again the MaxEnt solution Eq.7, only the meaning of x- and y-coordinate has been modified as indicated in fig.2. We denote signals and viewing-chords of the first camera by x and those of the second camera by y. We then enumerate the viewing-chords as depicted in fig.2. The pixel-geometry is chosen according to the mesh provided by the intersecting viewing-chords. The pixel, at which viewing-chord C_i^x and C_j^y intersect has coordinates (i, j). Actually, the approximation Eq.5 is not entirely correct in the present case, as it ignores the fact that the lengths of the line-segments in the different pixels differ, leading to a variation in the matrix elements g_{li} by about 50%.

The product form is retained even if we include experimental errors. Anticipating the result of the next section, the MaxEnt solution of the tomography problem for the fan-geometry, including experimental errors, in the line-integral approximations Eq.2 reads

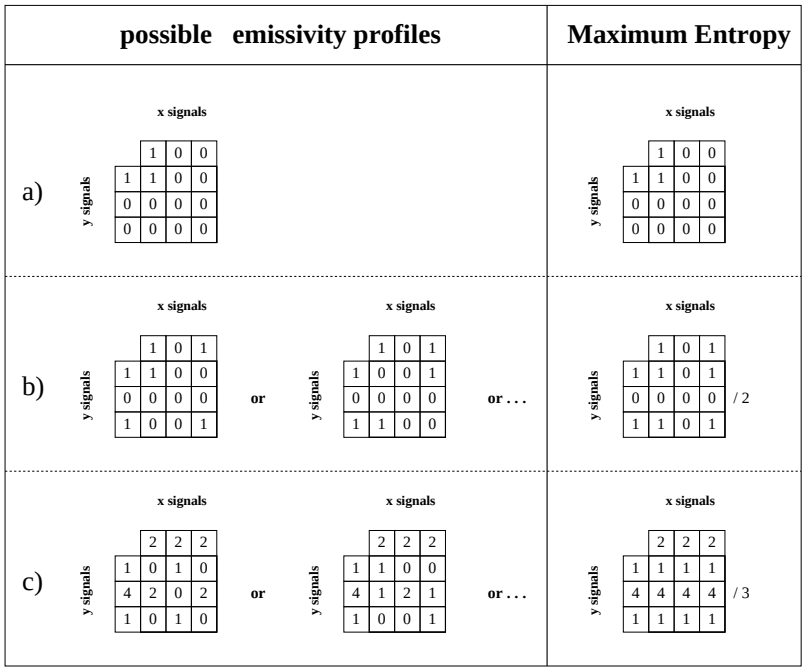

Table 1: *Demonstration of angular resolution in two-angle viewing geometry. Left hand columns and top rows of each table depict the x- and y-detector signals. The inner 3x3 block represents emissivities.*

again

$$E_{ij} \propto \tilde{p}_i^x \tilde{p}_j^y \qquad , \tag{8}$$

however, the $\tilde{p}_i$ are no longer the bare experimental signals.

3. Real world data and quantified MaxEnt

We are now prepared to tackle the tomography problem in full complexity, i.e. to invert Eq.1 consistently accounting for the statistical measurement errors. To this end, we invoke quantified MaxEnt[6, 7]. The *Likelihood* function assuming Gaussian error statistics reads

$$P(S|E,\sigma) = e^{-\frac{1}{2}\chi^2} \; ; \; \chi^2 = \sum_{l=1}^{N_d} (\frac{S_l - S_l(E)}{\sigma_l})^2 \qquad . \tag{9}$$

According to Eq.1 $S_l(E)$ is the predicted detector signal for given emissivity E. The entropy, entering the Prior $P(S|\alpha, m)$,

$$\mathcal{S} = \sum_i E_i - m_i - E_i \ln(E_i/m_i) \tag{10}$$

is measured relative to a default model m. For notational simplicity we have used a combined index i for x- and y-coordinate. The default-model plays a central role in the tomography problem and will be discussed in some detail. Above all, it is crucial to fully account

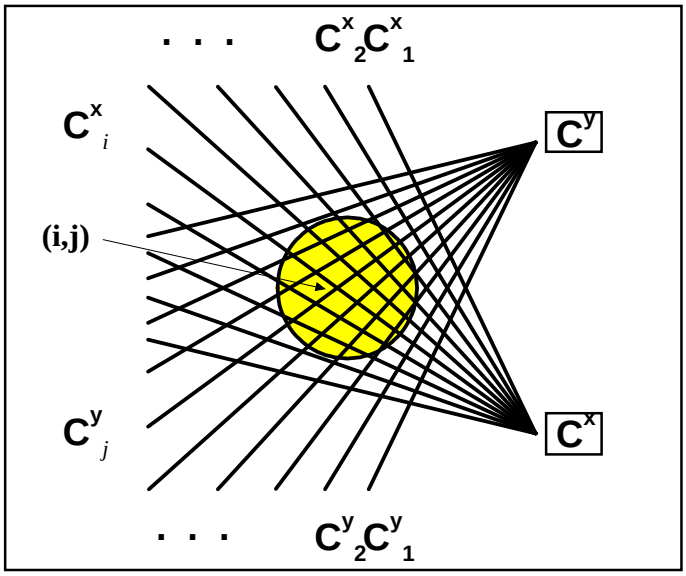

Figure 2: *Viewing geometry in W7AS. For clarity, only 10 viewing chords are depicted covering the same angular region as the 72 viewing chords given in the experiment.* C_i^α *represents the line of sight of camera* α *belonging to detector* i*. The arrow indicates pixel* (ij) *intersected by the view chords* C_i^x *and* C_j^y*, respectively.*

for our prior knowledge that the plasma is confined to the region, where the viewing chords intersect. Quantified MaxEnt can be mapped onto a dual problem [8] upon introducing a Legendre transform. The original 'potential energy' to be minimized reads

$$\phi(E,S) = \frac{1}{2}\chi^2 - \alpha\mathcal{S} = \frac{1}{2}\sum_l \frac{(S_l - S_l(E))^2}{\sigma_l^2} - \alpha\mathcal{S} \qquad . \tag{11}$$

We introduce the Legendre transform

$$\alpha\lambda_l \;:=\; \frac{\partial\phi}{\partial S_l} = \frac{(S_l - S_l(E))}{\sigma_l^2} \tag{12}$$

$$\Psi(E,\lambda) \;=\; \phi(E,S(\lambda)) - \alpha\sum_l \lambda_l S_l = -\frac{\alpha^2}{2}\sum_l \lambda_l^2\sigma_l^2 - \alpha\sum_l \lambda_l S_l(E) - \alpha\mathcal{S} \qquad . \tag{13}$$

The sought-for emissivity is readily obtained via the Euler-Lagrange equation

$$E_i = m_i e^{\sum_l \lambda_l g_{li}} \qquad . \tag{14}$$

The Lagrange parameters λ_l follow from Eq.12. The result, given in Eq.8, is a special case of Eq.14 if the data constraints Eq.5 are used. The regularization parameter α is determined upon maximizing the marginal posterior $P(\alpha|S,m,\sigma)$.

The idea of solving the plasma tomography problem by MaxEnt traces back to Frieden [9] and was applied in the sequel to H_α-tomography[10] and soft X-ray tomography for tokamak data[11]. The application to stellerator emissivities obtained by W7AS is more challenging as the emissivity profile is more structured and fewer experimental data are available. The MaxEnt concept offers several important advantages over other reconstruction techniques employed over the years, like those based on generalized Abel inversion [12, 13, 14, 15], linear least-squares techniques[16] and restricted Fourier analysis [1, 2, 3, 4]. It allows the reconstruction of arbitrary asymmetrical emissivity-profiles without any assumptions or restrictions which are tacitly made in the other approaches. This is particularly desirable if no independent experimental evidence is given to justify these restrictions. If, on the other hand, the assumptions are valid or if additional prior knowledge is given it can effectively be incorporated into the MaxEnt algorithm, leading to a systematic improvement of the results.

For completeness we mention the geometry parameters used in our calculation. In W7AS the plasma diameter is about 30cm . The reconstruction is performed on a square region of about 40cm$\times$40cm which is divided into 34×34 pixels, yielding a spatial resolution of 1.5 cm. The total angle, covered by the detectors of one pinhole camera (see fig.2), is about 40°. The system is highly underdetermined as the number of pixels is about 700 – only pixels with non-zero default model enter the calculation – while the number of detectors is 72. Moreover, the relevant plasma cross section is not sampled evenly, because both cameras are located on one side of the plasma (fig.2). Consequently, the information density is lower on the remote side of the detectors, leading to "shadow-effects" in the sense that the reconstructed profile will be more reliable close to the detectors than away from them. Needless to mention that this is a generic feature of the experimental set-up [15].

First we present results for synthetic data to illustrate the degree of reliability inherent to the MaxEnt reconstruction. Fig.3a shows the sample emissivity that sketches an m=4 MHD mode. The respective detector signals are computed via Eq.1 and adding 3% Gaussian noise. The MaxEnt reconstruction is shown in fig.3b. One finds a good overall agreement with the underlying "exact" image. But we observe also the expected shadow-effect, a decline in reliability with increasing distance from the detector. It is related to the decreasing information content of the chord-measurements for these parts of the plasma cross section. The m=4 symmetry is, however, clearly visible in the reconstructed image. We have repeated the reconstruction for the emissivity profile rotated around the poloidal axis. It appears that the quality gradually degrades with increasing rotation angle up to $\approx 45°$ after which it starts improving again. At $\approx 45°$ the peaks of the m=4 structure are pairwise lined up in the central viewing chords of the two cameras and the experiment provides no information, whatsoever, to resolve the m=4 mode[15]. Consequently, the MaxEnt reconstruction exhibits a single broad peak in the center of the plasma, like in example c) of table 1.

As a real world application, we reconstructed emissivity profiles from soft X-ray chord measurements on W7AS for a series of snapshots at consecutive times. A representative emissivity profile is depicted in fig.4a, which was obtain by quantified MaxEnt using a flat default model. As mentioned earlier, the default model was confined to the region of crossing viewing-chords. The reconstruction of a time series of emissivity profiles allows to observe the temporal changes in shape and position of the plasma profile, as well as the appearance,

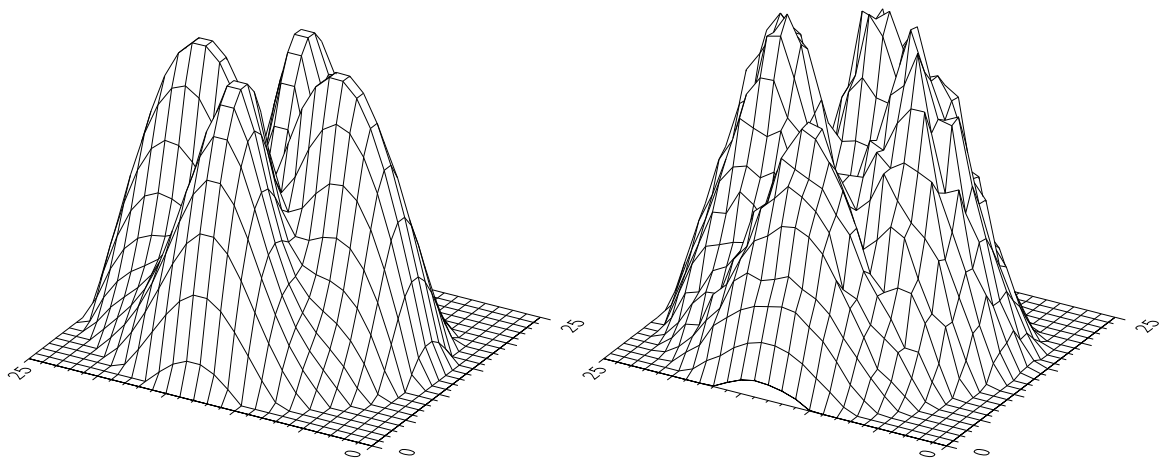

Figure 3: *Test tomography problem. Left) Synthetic tomography data, right) MaxEnt reconstruction, assuming a flat default model.*

motion, locking, and disappearance of magneto-hydrodynamic modes. We mentioned above that the resolution-quality of the reconstructed emissivity changes periodically, depending on the relative position of image-structures to the two cameras. The analysis of time sequences allows to bridge reconstructions of poor quality. It can be observed in fig.3a that the reconstruction is rather spiky, due to the exaggeratedly ignorant default model. The data demand strong deviations from the model resulting in a small regularization parameter. At the state of knowledge, expressed by the flat default model, MaxEnt cares first of all about the gross structure. Details are only tackled, if the coarse structure is already correctly provided by the default model. This is illustrated in fig3b. by the result for a default model, derived from the vacuum magnetic flux[15], which represents a reasonable prior knowledge. The default model has a bell-shape, the position of which is unknown and is treated as hyper-parameter. In Fig.4a the evidence (log-marginal-posterior) for the x-coordinate of the position is depicted. Even on a logarithmic scale the probability is sharply peaked. Fig.4b shows the response of the reconstruction to the position of the default model summarized by the center of mass and the maximum of the emissivity profile, respectively. It is good to see that the result depends only weekly on the position of the default model; the center of mass follows hesitantly the position of the default model, while the maximum even shifts slightly to the opposite direction. The reason lies in the fact that the "shadow" decreases with increasing shift in positive x-direction.

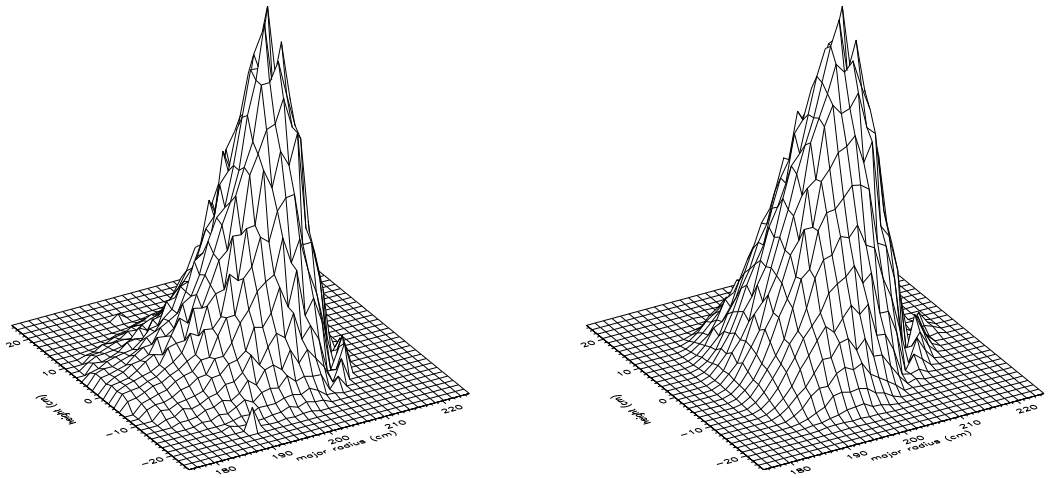

Figure 4: *Emissivity profile reconstructed from W7AS tomography data. left) flat default model right) bell-shaped default model.*

4. Summary

In summary, we have demonstrated that MaxEnt is perfectly suited to reconstruct emissivity profiles from X-ray chord-measurements irrespective of the detailed shape of the plasma. It is therefore more favorable than other reconstruction methods which depend crucially on the spatial smoothness of the image. MaxEnt provides a consistent description of probabilistic inference based on Bayesian statistics. It yields the most probable and noncommittal solution consistent with available noisy data and additional prior knowledge. It should be mentioned that MaxEnt allows to assign confidence intervals to the position and shape of the reconstructed image. This information is extremely valuable in the present case of week data-constraints to assess the predictive power of X-ray tomography, in general. Along the same lines of probabilistic inference it is possible to allow for different camera-sensitivities which are probably present. MaxEnt provides systematic and controlled means to incorporate justified assumptions (prior knowledge) thus restricting the image-space and yielding more informative (detailed) and more reliable results.

References

[1] A.P.Navarro, V.K. Paré, and J.L. Dunlap, Rev.Sci.Instrum. **52**, 1634 (1981).

[2] R.S. Granetz and J. Camacho, Nucl. Fusion **25**, 727 (1985).

[3] J. Camacho and R.S. Granetz, Rev.Sci.Instrum. **57**, 417 (1986).

[4] N.R. Sauthoff,K.M. McGuire, and S. von Goeler, Rev.Sci.Instrum. **57**, 2139 (1986).

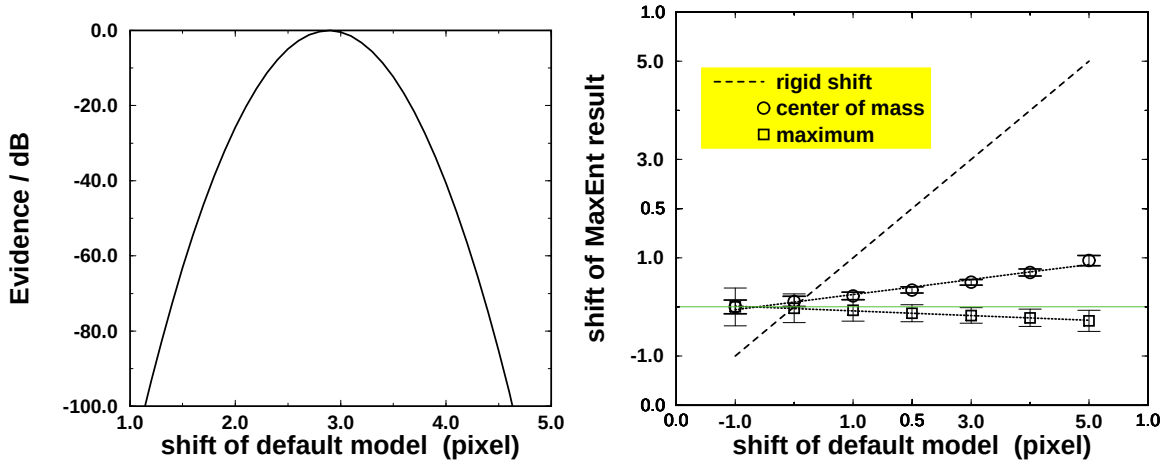

Figure 5: *The default model is shifted rigidly along the x-axis in pixel-units. a) (left) dependence of the evidence on the shift. b) (right) response of the center of mass and maximum-position of the emissivity profile.*

[5] E.T. Jaynes, (1958).

[6] S.F. Gull, in *Maximum Entropy and Bayesian Methods* ed. J. Skilling, (Kluwer, Academic Publishers, 1989).

[7] J. Skilling, in *Maximum Entropy and Bayesian Methods* ed. P. F. Fougère, (Kluwer, Academic Publishers, 1990).

[8] R. Silver, in *Maximum Entropy and Bayesian Methods* ed. G. Heidbreder, (Kluwer, Academic Publishers, 1993), to be published.

[9] B. Roy Frieden, J. Opt.Soc.Am. **62**, 511 (1972).

[10] G.A.Cottrell, in *Maximum Entropy in Action*, ed. B. Buck and V. A. Macaulay, (Oxford Science Publications, Oxford, 1990).

[11] A. Holland and G.A.Navrati, Rev.Sci.Instrum. **57**, 1557 (1986).

[12] K. Bockasten, J.Opt.Soc.Amer. **51**, 943 (1961).

[13] N.R. Sauthoff, S. von Goeler, and W. Stodiek, Nucl. Fusion **18**, 1445 (1978).

[14] N.R. Sauthoff and S. von Goeler, IEEE Trans.Plasma.Sci. **7**, 141 (1979).

[15] A.P. Navarro, M.A. Ochando, and A. Weller, IEEE Trans. on Plasma Science **19**, 569 (1991).

[16] R. Decoste, Rev.Sci.Instrum. **56**, 807 (1985).